Northumbria Research Link

Field effect transistor sensors based on in-plane 1T´/2H/1T´ MoTe2 heterophases with superior sensitivity and output signals

Shichao Zhang, You Wu, Feng Gao, Huiming Shang, Jia Zhang, Zhonghua Li, YongQing Fu, and PingAn Hu*

S. Zhang, Y Wu, H. Shang, Prof. Z. Li, Prof. P.A. Hu.
School of Chemistry and Chemical Engineering,
Harbin Institute of Technology,
Harbin 150080, China.
E-mail: hupa@hit.edu.cn

S. Zhang, Y Wu, F. Gao, H. Shang, Prof. J. Zhang, Prof. Z. Li, Prof. P.A. Hu.
MOE Key Lab of Micro-System and Micro-Structures Manufacturing,
Harbin Institute of Technology,
Harbin 150080, China.

Prof. Y.Q. Fu
Faculty of Engineering & Environment, Northumbria University, Newcastle upon Tyne, NE1 8ST, UK

Prof. P.A. Hu.
State Key Laboratory of Robotics and System,
Harbin Institute of Technology,
Harbin 150080, China.

Abstract

Two-dimensional (2D) materials, with their extraordinary physical and chemical properties, have gained extensive interest for physical, chemical and biological sensing applications. However, 2D material-based devices, such as field effect transistors (FETs) often show high contact resistance and low output signals, which severely affect their sensing performance. In this study, we develop a new strategy to combine metallic and semiconducting polymorphs of transition-metal dichalcogenides (TMDCs) to solve this critical issue. We applied a phase engineering methodology to integrate large-scale and spatially assembled multilayers of 2H $MoTe_2$ FETs with coplanar metallic 1T′$MoTe_2$ contacts. Such in-plane heterophase based FETs exhibit an ohmic contact behavior with an extremely low contact resistance due to the coplanar and seamless connections between 2H and 1T′ phases of $MoTe_2$. These 1T′/2H/1T′ based FETs were successfully demonstrated for detecting NH_3 with current outputs increased up to microamp levels without using any conventional interdigital electrodes, which is compatible with the current CMOS circuits for practical applications. Furthermore, the as-fabricated sensor can detect NH_3 gas concentrations down to 5 ppm at room temperature. Our research demonstrates a new strategy of applying the heterophase $MoTe_2$ based nanoelectronics for high-performance sensing applications.

1. Introduction

In the past a few decades, there has been a growing demand for highly sensitive and portable sensors capable of detection for traces of poisonous gases[1]. Attributed to their high surface-to-volume ratio, nanomaterials show great potentials for ultrasensitive chemical sensors with minimal dimensions and high packing densities[2]. A number of

nanomaterials, including carbon nanotubes[3], graphene (or reduced graphene oxides)[4], and two dimensional (2D) transition-metal dichalcogenides (TMDCs)[5] exhibit exceptional sensitivities to a wide variety of gas molecules, when these nanomaterials are used as the sensing layers.

Among these nanomaterials, 2D TMDCs have received considerable attention owing to their large surface-to-volume ratios, appropriate bandgaps, and suitable surface adsorption energies for gas molecules[5]. Up to now, 2D TMDCs such as MoS_2[6], $MoSe_2$[7], WS_2[8], and WSe_2[9] have been explored as gas sensing materials, but these 2D TMDCs based gas sensors often suffer from low-output signals, especially when operated at room temperature. Numerous devices have output currents only in the nanoampere range or even picoampere range[6], thus additional signal amplifiers are often required for the practical applications due to these weak signals. This results in a significantly increased complexity and high costs of devices. The significant constraint for these 2D TMDCs is their high resistance when contacted with the conventional metal electrodes. Despite that some suitable metals can be selected to minimize the barrier height at the interfaces between metal and 2D TMDCs, the metal-induced gap states are often generated, resulting in the pinning of Fermi-level and a substantially invariable Schottky barrier (SB)[10]. The conventional doping approach which are commonly employed in silicon technology cannot be easily applied into these 2D materials due to their atomic layer thickness. Recently, integration of 2D semiconductors with coplanar 2D conductors has shown great potentials in reducing their high contact resistance[11]. However, many of these approaches are not suitable for large scale productions[12] and the interfaces between 1T′ phase and 2H phase of the 2D TMDCs often show overlapped flakes or incomplete stitches[11b, 13]. Hence, a new

strategy of selectively regulating the coplanar interfaces between these 2D semiconductor and metal is critically needed for sensing applications.

Herein, we introduce a new strategy of realizing spatially selective assembly of 2H MoTe$_2$ and 1T′ MoTe$_2$ based on a phase-selective growth method. Large-scale and heterophase of MoTe$_2$ based field effect transistor (FET) array is fabricated, and the obtained 1T′/2H/1T′ MoTe$_2$ FET exhibits a low contact resistance of ∼7.1 kΩ μm under an on-state voltage of -60 V. When used for electronic devices, this FET generates current signals as large as microamperes without using any interdigital electrodes, thus additional amplification is not required for these applications. The device exhibits a high sensitivity for gas sensing, and can detect as low as 5 ppm of NH$_3$, along with fast response and recovery times (43/19 s) operated at room temperature. The fabrication process and measurement of the FET sensor are compatible with the current CMOS process. This work provides a new strategy on fabricating CMOS-compatible, high current signal, and large-area gas sensors based on the 2D materials.

2. Results and discussion

2.1 Synthesis strategies of MoTe$_2$ heterophases

Figure S1 shows the proposed synthesis strategies for pure metallic and semiconducting phases of MoTe$_2$, both of which require the specific molybdenum precursors[14]. The precursor for 1T′ MoTe$_2$ growth is a continuous Mo film prepared by electron beam evaporation, whereas the precursor for 2H MoTe$_2$ growth is MoO$_3$ film, which is prepared by treating Mo film with oxygen plasma. Then the obtained precursors are tellurized, which is heated to 700 °C for 2 h with a mixed hydrogen and argon gases (Ar/H$_2$ 15/15 sccm in gas flow). Hydrogen is essential for the growth of MoTe$_2$, because the tellurization process requires a reducing environment. After

tellurization, continuous films of pure 1T´and 2H MoTe$_2$ are obtained. The crucial

parameters to control the phases of MoTe$_2$ grown from precursors are the Te

concentration and the strain condition in the MoTe$_2$ crystal[15]. Theoretical calculation

predicts that 1T´ MoTe$_2$ is stable under a certain strain whereas 2H MoTe$_2$ is stable

without applying any strain.[16] For the reactions based on Mo precursor, stress

condition is the main factor determining the phase of MoTe$_2$. With the change of the

unit cell volume from Mo (15.48 Å^3) to MoTe$_2$ (224.62 Å^3)[16], a large strain is induced

during the tellurization process. The 1T´ phase is the stable phase after prolonging the

reaction time. To be compared with, for the reaction based on MoO$_3$ precursor, the

change of the unit cell volume from MoO$_3$ (202.99 Å^3) to MoTe$_2$ (224.62 Å^3) is much

smaller[16]. As we known, the strain induced can be released during the tellurization

process. Therefore, the Te concentration is the main factor determining the phase of

MoTe$_2$. The average ratio of Mo:Te in the 2H phase obtained from the MoO$_3$ precursor

is 1:2.07, which is slightly higher than 1:2. However, for the 1T´ MoTe$_2$ obtained from

the MoO$_3$ precursor with a shortened reaction time, the average ratio of Mo:Te is 1:1.93,

which is less than 1:2. During its reaction with MoO$_3$ precursor, the 1T´ phase is

transformed into 2H phase during which the Te vacancies are re-occupied.

The optical contrast of the 1T´ MoTe$_2$ film is quite different from that of the 2H MoTe$_2$,

indicating that these two films have distinctly different properties (Figure S2). Based

on a phase-selective growth method, continuous films with a few-layer 2H/1T´ MoTe$_2$

with desired patterns can be obtained (Figure S3). The procedures for preparing lateral

heterophases of MoTe$_2$ structures are schematically shown in Figure 1.

Photolithography and electron beam evaporation are used to prepare patterns of Mo

film (5 nm) on a SiO$_2$/Si substrate (Figure 1a). Photolithography process is further used

to create selectively exposed areas on Mo film (Figure 1b), and then after oxygen plasma treatment, the exposed region is converted into molybdenum oxide (MoO_3) (Figure 1c). The differences of optical contrast between the oxidized and unoxidized Mo films reveal a homogeneous transformation of materials. To grow the lateral structure of 2H/1T´ $MoTe_2$, molybdenum precursors are tellurized under the same conditions as above. Polycrystalline 2H/1T´ $MoTe_2$ films are formed on Mo/MoO_3 films after the tellurization process, as shown in Figure 1d.
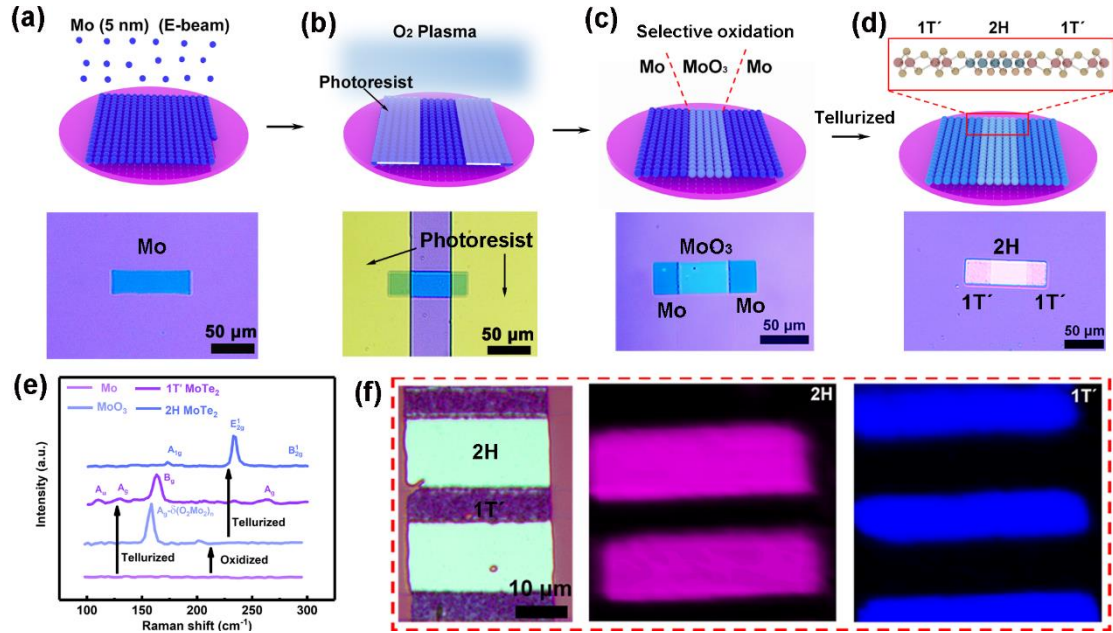
Figure 1. Schematic illustrations of the fabrication processes of the chemical assembly processes of 2H/1T´ heterophase $MoTe_2$. (a-d) Fabrication processes of 2H/1T´ heterophase $MoTe_2$. (e) The evolution of Raman spectroscopy from Mo precursors to $MoTe_2$. (f) Optical image and corresponding Raman mappings at 233 cm^{-1} (E_{2g}^1 mode of 2H phase) and 161 cm^{-1} (B_g mode of 1T´phase) of the 2H/1T´ interface.

Figure 1e depicts the evolution of Raman spectra from that of molybdenum precursors to $MoTe_2$. For the Mo film, no Raman peaks were found as expected. Following the oxidation, Raman peaks at 158 (A_g-$(O_2Mo_2)_n$) and 201 cm^{-1} are emerged and they are

assigned to the characteristic peaks of MoO_3[17]. After the tellurization process, Raman peaks of 1T′ $MoTe_2$ located at 110 cm^{-1}(A_u), 130 cm^{-1}(A_g), 163 cm^{-1}(B_g), and 261 cm^{-1}(A_g) are observed[18], with the dominant peak at 163 cm^{-1}(B_g). 2H $MoTe_2$ exhibits typical Raman peaks at 173 cm^{-1}(A_{1g}), 233 cm^{-1}(E_{2g}^1), and 291 cm^{-1}(B_{2g}^1), with a dominant peak at 233 cm^{-1}(E_{2g}^1).

Figure S4 reveals the peak evolutions of Mo 3d core levels from Mo precursors to $MoTe_2$, obtained from an X-ray photoelectron spectroscope (XPS). For Mo metal precursor, the peaks at 227.75 and 231.05 eV are classified as those of Mo $3d_{5/2}$ and $3d_{3/2}$ levels, respectively. After O_2 plasma treatment, peaks of Mo $3d_{5/2}$ and $3d_{3/2}$ level are shifted to 232.40 and 235.55 eV, respectively. The redshift of the binding energy reveals that the oxidation treatment is an electron loss process, and the Mo precursor is oxidized. For the 2H $MoTe_2$, two peaks at 228.5 and 231.7 eV are classified as those of Mo $3d_{5/2}$ and $3d_{3/2}$ ones, whereas those at 228.1 eV (Mo $3d_{5/2}$) and 231.3 eV (Mo $3d_{3/2}$) are linked to 1T′ $MoTe_2$, respectively. In addition, the existence of Te is confirmed by the XPS survey spectra of both the as-synthesized 2H and 1T′ $MoTe_2$ (Figure S5). The XPS peaks of 2H $MoTe_2$ are at 572.95 eV (Te $3d_{5/2}$) and 583.35 eV (Te $3d_{3/2}$), whereas those of 1T′ $MoTe_2$ are at 572.70 eV (Te $3d_{5/2}$) and 583.10 eV (Te $3d_{3/2}$), respectively. Results clearly show that the binding energy of 1T′ $MoTe_2$ peaks is 0.1-0.4 eV smaller than that of 2H $MoTe_2$, which was also reported in literature[15, 19].

Figure S6 shows a schematic model of the in-plane heterophase interface[20]. It possesses a trigonal prismatic structure of the 2H phase and a distorted octahedral shape of the 1 T′ phase. The surface properties of 2H/1T′ $MoTe_2$ were further studied using an atomic force microscope (AFM, as shown in Figure S7). Both of these two phases

show an approximative thickness of ~12.5 nm, which was achieved by the accurate control of Mo film thickness. The roughness of the 2H $MoTe_2$ surface is ~1.6 nm. Compared with the 2H $MoTe_2$, the 1T′ $MoTe_2$ synthesized from the Mo precursor is significantly rougher, e.g., with a value of ~8.1 nm. Due to the high melting point of molybdenum (2620 °C), Mo atoms cannot migrate freely on the surface of substrate at the reaction temperature. Thus, the as-grown $MoTe_2$ exhibits a higher surface roughness[14a]. The spatial distribution of the heterophase $MoTe_2$ interface has been characterized using both the optical image and Raman mapping (Figure 1f) for both the 2H $MoTe_2$ E_{2g}^1 mode and the 1T′ $MoTe_2$ B_g mode. Results clearly show that these two phases exhibit uniformly optical contrast, and thus are homogeneously distributed.

Crystallographic structure of the in-plane $MoTe_2$ heterophase was investigated using a transmission electron microscope (TEM). Using a PMMA-assisted transfer approach and the hydrofluoric acid as an etchant[21], $MoTe_2$ samples were transferred onto a copper grid. Figure 2a shows a dark-field TEM image of the in-plane $MoTe_2$ heterophase, which consists of three regions, region I (bright area, 2H phase), region II (penumbra area, 2H/1T′ interface), and region III (dark area, 1T′ phase). Figure 2b shows a high-resolution TEM (HR-TEM) image of region I, in which the 0.35 nm lattice spacing is corresponding to the (004) orientation of 2H $MoTe_2$[18]. The inset image of Figure 2b shows the selected area electron diffraction (SAED) pattern of the region I, revealing the same-orientation hexagonal patterns of 2H $MoTe_2$. Figure 2c shows a TEM image of interfacial region of the 1T′/2H $MoTe_2$ heterophase, clearly revealing the atomic-scale transition from the 1T′ phase to the 2H phase. The inset image of Figure 2c shows the SAED of the 2H/1T′ interface, in which both the diffraction spots with 6-fold symmetry (2H $MoTe_2$) and diffraction rings (1T′ $MoTe_2$) are observed[11a].

Figure 2d shows a high-resolution TEM (HR-TEM) image of region III, which reveals a monoclinic 1T′ structure as expected. The monoclinic crystal lattice with an interplanar spacing of 0.63 nm is corresponding to the (100) plane of monoclinic 1T′ structure. The inset image in Figure 2d shows that the corresponding SAED patterns with many diffraction rings are corresponding to those of the 1T′ structure[22].
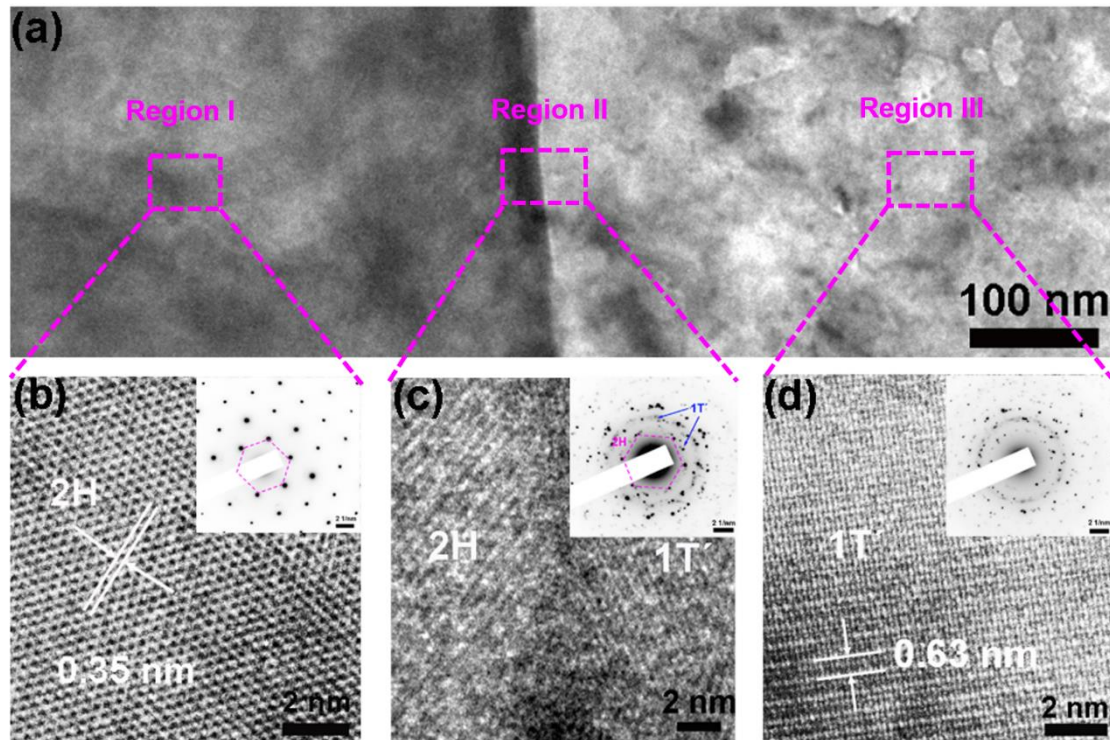
Figure 2. TEM characterizations of the MoTe₂ heterophase interface. (a) TEM images of the in-plane 1T′/2H MoTe₂ homojunction structure at low magnification. (b-d) HR-TEM image of the 2H MoTe₂ (b), the in-plane 1T′/2H MoTe₂ heterophase region (c), and the 1T′ MoTe₂ (d); inset: the corresponding SAED pattern.

2.2 Electrical characteristics of MoTe₂ devices

To characterize electrical properties of the MoTe₂ heterophase, 1T′/2H/1T′ and 2H-only MoTe₂ FET devices were fabricated. Figure 3a depicts an optical image of a 1T′/2H/1T′ FET array, in which the amplified part is a single device. Pd electrodes of

40 nm thick were patterned onto the metallic phase sections of each 1T´/2H/1T´ MoTe$_2$ structure using the conventional photolithography and thermal evaporation processes. For comparisons, the 2H-only devices with 40 nm Pd electrode were also fabricated.

Figure 3b shows the room temperature output curves of the 1T´/2H/1T´ and 2H-only FET devices, both of which display a linear behavior. At the same value of the source-drain voltage (V_{ds}), the source-drain current (I_{ds}) value of the 1T´/2H/1T´ device is 11 times higher than that of the 2H-only device. This indicates that the 1T´/2H/1T´ device possesses a lower contact resistance than the 2H-only device. Figure 3c shows transfer curves (I_{ds} vs V_{gs}) of these two types of devices at a V_{ds} of 1 V at room temperature. The corresponding carrier motilities of the MoTe$_2$ FETs can be extracted from the following equation[23]:

$$\mu = \left(\frac{L}{WC_{ox}V_{ds}}\right)\left(\frac{dI_{ds}}{dV_{gs}}\right). \qquad (1)$$

where L is the channel length, W is the channel width, and C_{ox} is the gate capacitance per unit area. Both types of devices show a p-type semiconductor behavior based on the results shown in Figure 3c. The on/off current ratio of the 1T´/2H/1T´ device is 200 and the carrier mobility is 5.6 cm^2 V^{-1} s^{-1}, the latter of which is 8 times higher than that of the 2H-only FET (0.6 cm^2 V^{-1} s^{-1}).

Figure S8 shows the transfer characteristics (I_{ds} vs V_{gs}) of these two types of devices obtained at a V_{ds} of 1 V and various temperatures from 120 to 300 K. The current on/off ratios of the 1T´/2H/1T´ FET are changed substantially with the temperature, which suggests that the current of the 1T´/2H/1T´ FET is governed by a mobility-limited process rather than a thermionic one[12b]. The changes of the on/off ratios for the 2H-

only FETs are not significant, suggesting the current in this device is governed by the thermionic-limited mechanism[12b].
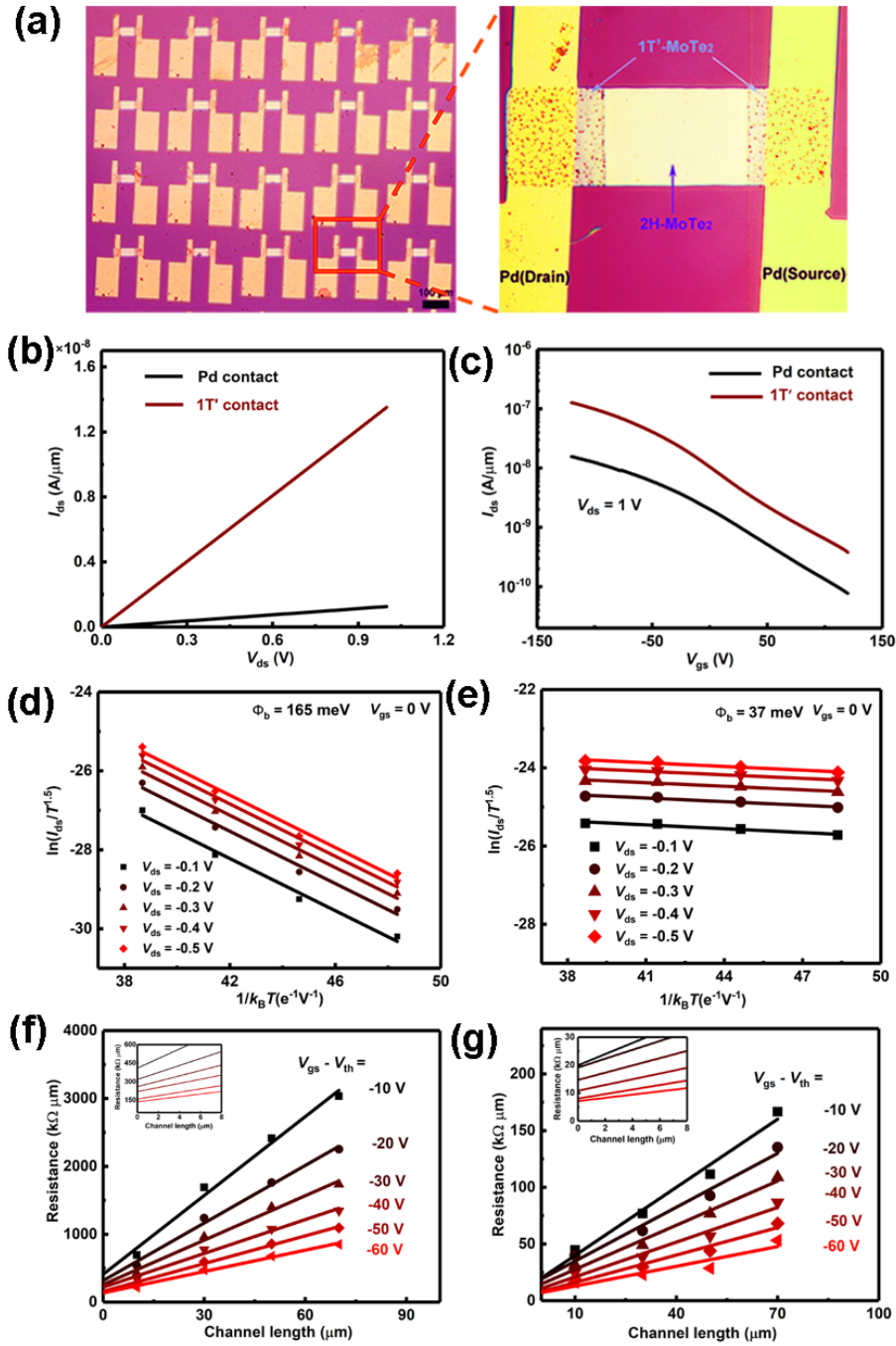
Figure 3. Comparisons of the electrical performances of simultaneously synthesized FETs and traditional fabricated FETs. (a) Optical micrograph of the heterophase MoTe$_2$ FET array. of the heterophase 1T´/2H/1T´ MoTe$_2$ FET array. (b) Room-temperature output curves of the 1T´/2H/1T´ and the 2H only device at V_{gs} = 0 V. (c) Room-temperature transfer curves of the 1T´/2H/1T´ and 2H only device at V_{ds} = 1 V. (d, e) Arrhenius plots for the 1T´/2H/1T´ (d) and the 2H-only device

(e) at V_{gs} = 0 V for different values of V_{ds}. (f, g) The total device resistance versus L at various V_{gs}-V_{th} of 1T´/2H/1T´ (f) and the 2H-only device (g).

The Arrhenius curves for a 2H-only FET obtained at V_{gs} of 0 V with the temperatures changed from 240 to 300 K are shown in Figure 3d. The Arrhenius plot has shown a negative slope, suggesting a positive activation energy[11a]. The obtained average Schottky barrier height (Φ_B) is 165 meV. The Arrhenius graphs for a 1T´/2H/1T´ FET at V_{gs} = 0 V at different temperatures from 240 to 300 K are shown in Figure 3e. Compared to those of the 2H-only FETs, smaller negative slopes of the Arrhenius plots are observed, indicating a smaller Schottky barrier height for the 1T´/2H/1T´ FETs, and the corresponding average Schottky barrier height (Φ_B) is 37 meV. This lower Schottky barrier value demonstrates the advantages of the 1T´/2H/1T´ devices for applications in electronics and nanoelectronic sensors.

In order to obtain the contact resistances R_c of these two types of devices, the transfer length method (TLM) was employed to extract the length-dependent resistance[11b]. These two types of MoTe2 FETs with various channel lengths are shown in Figure S9. Figure S10 shows the transfer curves obtained from the individual   1T´/2H/1T´and 2H only devices with various channel lengths. Figure 3f shows the total resistance versus channel length for the 2H-only FET at various V_g-V_{th} values. When a higher turn-on gate voltage was used, the minimum total R_c value was obtained to be ~138.3 kΩ μm. Figure 3g depicts the total resistance value versus channel length of a 1T´/2H/1T´ FET at different V_g-V_{th} values. At a higher turn-on gate voltage, the lowest total R_c value was extracted to be ~7.1 kΩ μm, which is one nineteenth of the 2H-only device. This value reveals that the 1T´/2H/1T´ FET device has a much lower barrier height than that of the 2H-only FET.

Table S1 summarizes the recently reported preparation methods, field-effect mobilities, integration levels and contact barriers of various FET devices based on MoTe$_2$. If compared with the performance of those reported references, our developed 1T′/2H MoTe$_2$ heterophase-contacted FETs have shown outstanding properties in terms of high values (including both in-plane and vertical configurations).

Figure S11 further displays the device performance statistics for the 2H only FETs device and the 1T′/2H/1T′ device, suggesting that the 1T′/2H MoTe$_2$ interface has a lower contact resistance. A Kelvin probe force microscopy (KPFM) image (Figure S12) and the obtained corresponding potential line profile confirm their potentials of 19.68 mV (2H MoTe$_2$/Pd) and 24.80 mV (1T′/2H MoTe$_2$).

To confirm the actual position of valence-band maximum for the multilayer 2H MoTe$_2$, XPS valence band spectra were obtained and the results are shown in Figure S13. It proves that E_f value is ≈ 0.22 eV above the valence-band maximum (E_v). Considering the bandgap of 1.05 eV[24], we can confirm that E_f resides in the bandgap's lower half region. Figures S14a and S14b show the illustrations of the band alignments for 2H MoTe$_2$/Pd vertical junction and 1T′/2H MoTe$_2$ in-plane heterostructure before contact, respectively. Figure S14c shows the illustration of band alignment of 2H MoTe$_2$/Pd surface contact based on the Schottky-Mott theory. It should be pointed out that interfacial energy states can cause the Schottky barrier height to be deviated from the Schottky-Mott theory (Figure S14d), through a process commonly known as Fermi level pinning[25]. Fermi level pinning of MoTe$_2$ is attributed to the Te vacancies, interface dipoles resulted from charge redistribution, orbital overlap, negative

ionization of the outmost Te atom complex, and intrinsic MoTe$_2$ surface defects and gap states induced in the van der Waals gap[25]. The 1D 1T′ MoTe$_2$ edge contacts are free from the multiple origins of the Fermi level pinning, therfore, the 1T′/2H/1T′ MoTe$_2$ heterostructure has a much lower contact resistance than that of the Pd/2H MoTe$_2$/Pd structure as shown in Figure S14e.

2.3 Gas sensing characteristics of MoTe$_2$ devices

Recently, nanoelectronic gas sensors based on 2D TMDCs have been widely studied[26], as their large surface-to-volume ratios significantly enhance efficient adsorption, diffusion and release of the detected gas molecules[27]. To demonstrate the sensing performance, we use different types of MoTe$_2$ FET devices for sensing ammonia molecules. Figure 4a depicts the room temperature results of I_{ds} vs V_{ds} for both the 1T′/2H/1T′ and 2H-only sensors before and after exposure to 100 ppm NH$_3$. The working current of 1T′/2H/1T′ sensor is obtained at the microamp level before and after exposure. When exposed to 100 ppm NH$_3$, the source-drain current of the 1T′/2H/1T′ sensor is decreased by 0.32 A at V_{ds} = 1V, which is approximately three times larger than the 0.11 A of the 2H-only device. The sensitivity (S), defined as the proportional change in the drain current, is obtained using the following equation[28]:

$$S(\%) = \frac{(I_{gas-on} - I_{gas-off})}{I_{gas-off}} \times 100\% \qquad (2)$$

Where I_{gas-on} and $I_{gas-off}$ represent the collector's current in gas-exposed condition and in air, respectively. The responses of 1T′/2H/1T′ sensors to 100 ppm of NH$_3$ at room temperature are shown in Figure 4b. The exposure time is maintained at 70 s. Results demonstrate that this sensor shows a high response value (-17%), a fast response time (43 s), and a rapid recovery time (19 s), operated at ambient temperature.

To investigate the structural changes of our device after the gas sensing, we performed XPS analysis on 2H MoTe$_2$ film before and after used for the NH$_3$ sensing, and the obtained results are shown in Figure S15. A minor shift of binding energy (0.1 eV) for both Mo 3d$_{5/2}$ and Mo 3d$_{3/2}$ indicates that the Mo's chemical valance is altered, mainly due to the formation of coordinated ligands of NH$_3$ on Mo atoms at the position of Te vacancies[29].

For demonstration of practical applications of these two types of FET sensors, their stability and reproducibility were further studied. Figure 4c shows the responses of the 1T′/2H/1T′ and 2H-only sensors to 100 ppm NH$_3$ at room temperature. Both these two types of sensors can be operated for 7 cycles without notable changes in the responses. Figure 4d depicts NH$_3$ sensitivity results of the 1T′/2H/1T′ sensor. The test was carried out at room temperature with NH$_3$ concentrations varied from 5 to 500 ppm. Figure 4e depicts the relative responses of the 1T′/2H/1T′ device to various NH$_3$ concentrations. Results show that the 1T′/2H/1T′ sensor has relative response values of -1.39%, -1.70%, -3.05%, -8.00%, -10.75%, -17.30%, 22.13%, 26.18%, and 28.27% toward 5, 10, 15, 30, 50, 100, 200, 300, and 500 ppm of NH$_3$, respectively. The sensor shows rapid changes of its conductance upon exposure to low concentrations of NH$_3$. At high NH$_3$ concentrations, a quasi-saturation characteristic of responses is observed.

For practical applications, the gas sensors are often used in different gas environments. Consequently, a gas sensor's selectivity is one of its crucial sensing parameters. In order to determine the selectivity of the 1T′/2H/1T′ sensor, several gases including NH$_3$, ethanol, CO$_2$, H$_2$S and formaldehyde were measured with the same concentration of 500 ppm at room temperature. The measurement results are depicted in Figure S16.

Measurement results show that the gas responses of the 1T´/2H/1T´ sensor developed in this study against NH_3 (-28.81%) are significantly higher than those of the other gases, such as ethanol (-3.59%), CO_2 (-10.85%), H_2S (-2.19 %), and formaldehyde (-11.99%), which indicates the good selectivity of this 1T´/2H/1T´ sensor for ammonia. In addition to sensitivity, stability is another critical parameter for the gas sensor. Figure S17 further shows the stability results of the 1T´/2H/1T´ sensor exposed to 100 ppm NH_3 over a period of 8 days. The sensor's responses become stabilized over time, proving the 1T´/2H sensor's long-term stability.

Figure 4f compares the NH_3 sensing results of the 1T´/2H/1T´ sensor with those from recent representative NH_3 sensors made of $Ti_3C_2T_x$[30], SnO_2 nanoparticles[31], MoS_2/MoO_3[32], MoS_2[33], $NiWO_4/CNT$[34], WS_2[35], M-CNTs[36], $Cs_3Bi_2I_6Br_3$[37], and RGO/CuO[38]. The detection limit and operating current of our 1T´/2H/1T´ sensor outperform most of these reported NH_3 sensors. These findings demonstrate that 1T´/2H/1T´ $MoTe_2$ is an appealing candidate for 2D TMD-based FET sensors.
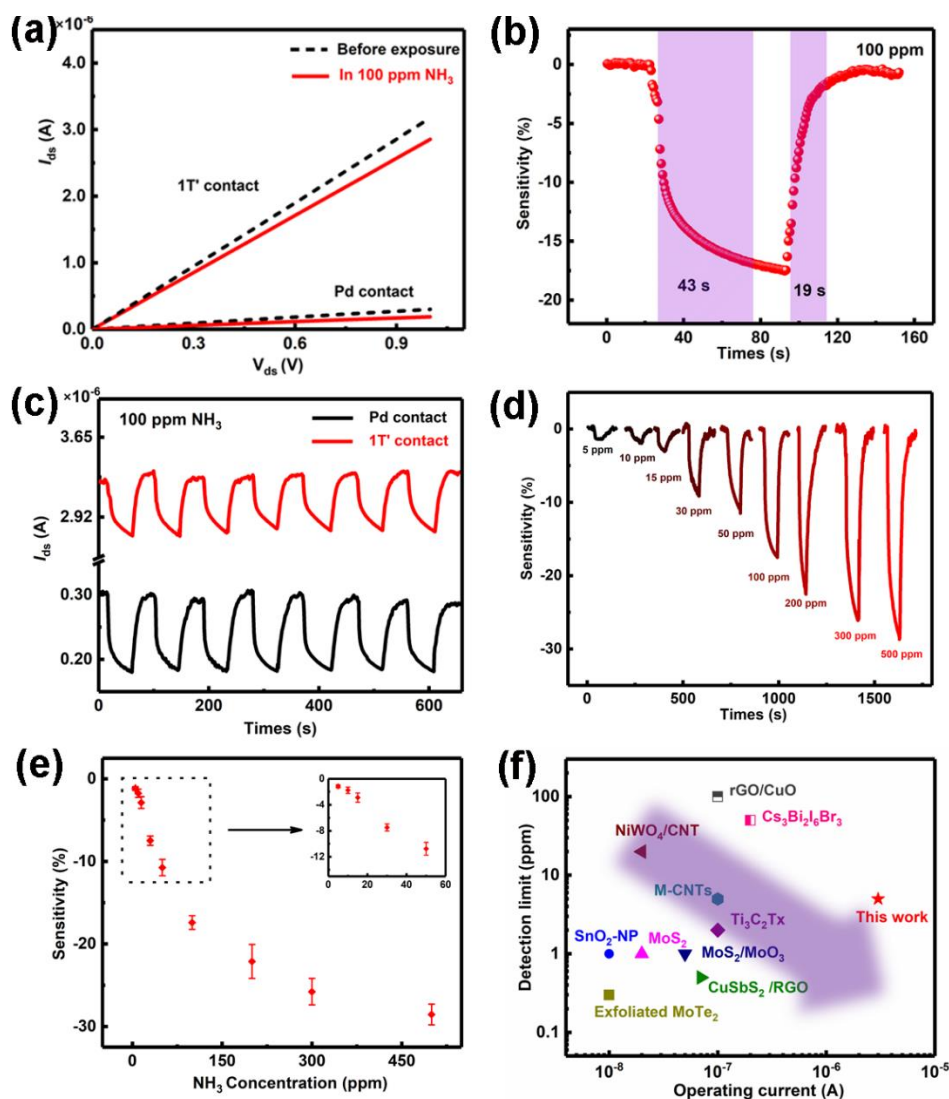
Figure 4. Gas sensing performance of the 1T'/2H/1T´MoTe₂ device. (a) Conductance change of the 1T'/2H/1T´and the 2H-only sensors upon exposure to 100 ppm. (b) Sensitivity of the 1T´/2H/1T´ MoTe₂ sensor to 100 ppm of NH₃ at room temperature. (c) The stability of the 1T'/2H/1T´and the 2H-only sensors to 100 ppm NH₃. (d) Sensitivity of the 1T'/2H/1T´ MoTe₂ sensor to different concentrations of NH₃. (e) Sensitivity change versus NH₃ concentration based on the 1T'/2H/1T´MoTe₂ sensor. (f) Detection limit and operating current from this work and previous reports.
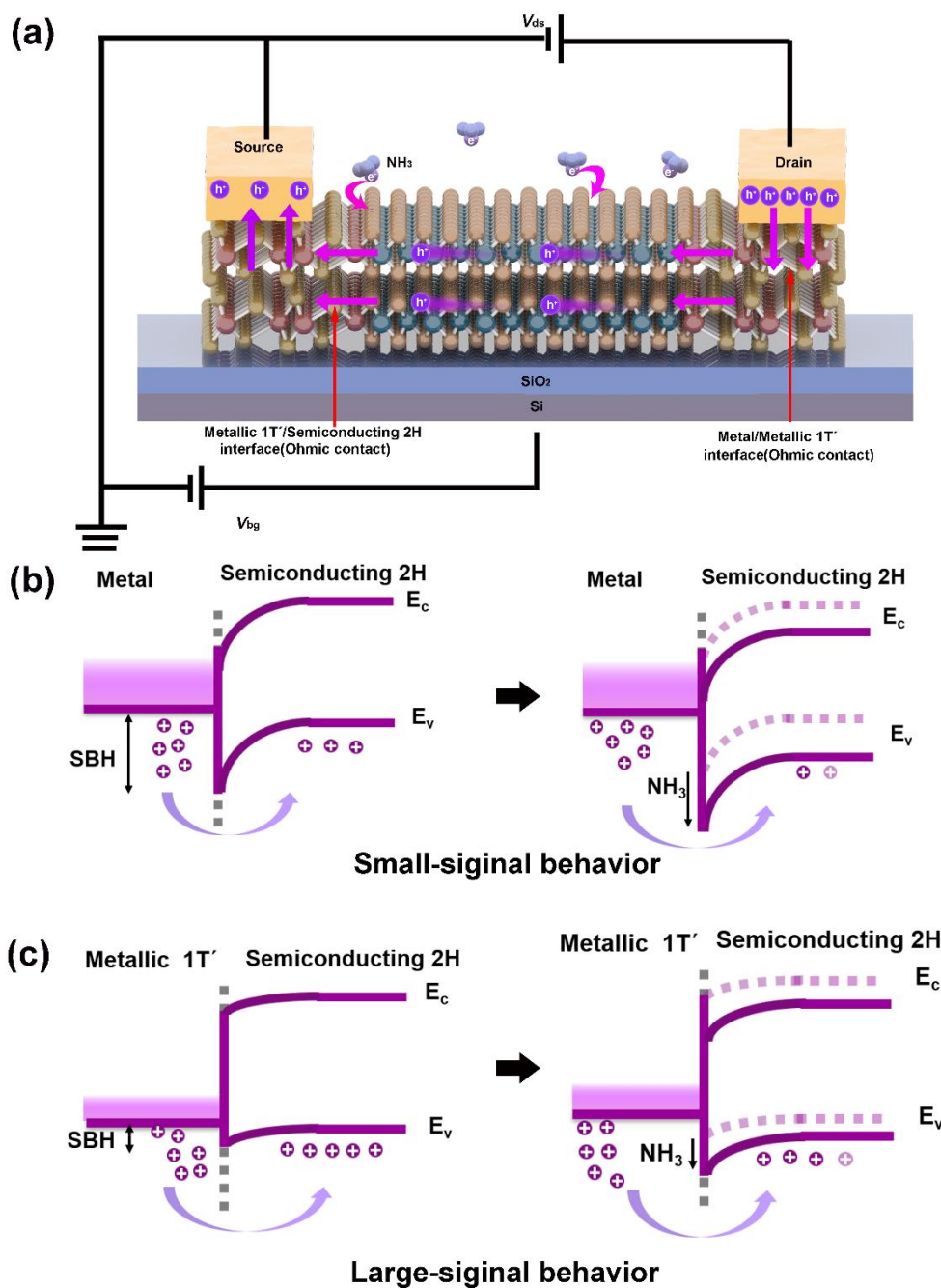
Figure 5. Schematic of sensing mechanism and energy band diagram of MoTe$_2$ devices. (a) Schematic illustration of the 1T′/2H/1T′ MoTe$_2$ sensor for vapor-phase NH$_3$ sensing. (b, c) Band structure diagram for of the 2H-only and the 1T′/2H/1T′ sensors before and after ammonia exposure.

2.4 Density Functional Theory Study

Using DFT simulations, we investigated the adsorption performance of NH$_3$, H$_2$S, and CO$_2$ molecules on the basal and edge Te vacancies of the (001) plane and specific lattice

planes of 1T′ and 2H MoTe$_2$ nanosheets[39]. Figure S18 displays their adsorption configurations. Table S2 lists the obtained adsorption energies of the NH$_3$, H$_2$S, and CO$_2$ molecules on the MoTe$_2$ surfaces. For the (001) plane of MoTe$_2$, the adsorption energies of gas molecules on the 1T′ phase are much larger than those on the 2H phase. Whereas the adsorption energies of the (101) lattice plane of the 1T′ phase are significantly lower than those of the (100) and (010) lattice planes of the 2H phase.

2.5 Structure and operating principle of MoTe$_2$ FET sensor

The good performance of the 1T′/2H/1T′ sensor is due to the low-resistance of planar 2H/1T′ heterostructure and polycrystalline properties of 2H MoTe$_2$. Figure 5a schematically illustrate the atomic layer structures of 1T′/2H/1T′ based gas sensor. Compared to the other types of gas sensors, our 1T′/2H/1T′ device possesses distinctive advantages. Firstly, the polycrystalline 2H MoTe$_2$ provides numerous defects, such as vacancies, edges, and grain boundaries, which play crucial roles in enhancing the response rate and sensitivity of a gas sensor[27]. Secondly, the low-resistance planar heterostructure can produce a large current output. The current can reach the microamp scale without a need for any interdigital electrodes, which indicates that no additional amplification of this device is required for their practical applications. Figures 5b and 5c show the band diagrams of the 2H MoTe$_2$ gas sensors with metal contact and 1T′ MoTe$_2$ contact, before and after the exposure to NH$_3$. As the NH$_3$ gas molecules are electron donors, when they are adsorbed onto the surfaces of 2H MoTe$_2$, the valence band level of 2H MoTe$_2$ is decreased[40]. Therefore, the Schottky barrier heights (SBH) are increased by the Schottky barrier modulation (SBM), making it difficult for the charger transfer. Thus, the output current of 2H-only sensors is quite low. Additional signal amplifiers are needed for the device to ensure the good outputs for the practical

applications. Whereas for the 1T´/2H/1T´ sensors, both high sensitivity and high output current can be maintained as shown in Figure 4d. These findings demonstrate that 1T´/2H/1T´ MoTe$_2$ is an excellent candidate for 2D TMD-based FET sensors.

3. Conclusion

In brief, we have demonstrated a large-scale selective growth of an integrated MoTe$_2$ heterophase structure and its FET sensors. In this MoTe$_2$ heterophase structure, the junctions between the 1T´ and 2H phase are seamlessly stitched. The 1T´/2H/1T´ MoTe$_2$ FETs exhibit an ohmic contact character with a low barrier height and low contact resistance. Large-scale FET arrays are fabricated, and the carrier mobility of the 1T´/2H/1T´ FET is remarkably larger than that of the 2H-only FET. The fabrication process is compatible to the current CMOS process. We apply the 1T´/2H/1T´ device for the NH$_3$ detection and demonstrated a high sensitivity, e.g., with a detected NH$_3$ levels as low as 5 ppm accompanied by faster response and recovery. Our selective growth of the integrated in-plane heterophase structures provide a new route toward industry compatible large-area 2D electronics and sensors.

4. Experiment Section

4.1 Synthesis of 2H/1T´ MoTe$_2$ lateral structure.

A new synthesis strategy was used to fabricate the 2H/1T´ MoTe$_2$ lateral structures (see Figure 1a-d). Firstly, standard cleaning methods were used to prepare a Si substrate coated with 300 nm SiO$_2$. Then Mo patterns (5 nm thick) were fabricated using standard photolithography and electron beam evaporation processes. The standard photolithography and oxygen plasma treatment were further employed to prepare selective oxidation zones in the Mo patterns. Finally, the in-plane heterophase MoTe$_2$ structure were obtained by tellurizing the Mo/MoO$_3$ films. During tellurization, 2.0 g

of high purity Te powder (99.95 percent, Alfa) was deposed at the upstream end of the inner single-ended sealing tube with a length of 130 mm and a diameter of 12 mm, placed 10 cm away from the central heat zone. The substrate with Mo/MoO_x films was inserted into the inner tube at the central heat zone. The system was heated to 700 °C in 40 min and then kept at 700 °C for another 120 min. During this process, a combination of H_2 (15 sccm) and Ar (15 sccm) gas fluxes was continuously flowing through the tube. The system was naturally cooled down to room temperature after the growth process.

4.2 Structure characterizations.

The shapes and sizes of the $MoTe_2$ samples were evaluated utilizing an optical microscope (Cnoptec, BK6000), and their surface topography images were obtained using an AFM (Bruker Dimension FastScan, Tapping mode). Raman spectra were obtained using a LabRAM XploRA with a wavelength of 532 nm. XPS characterization was carried out using an XPS (Thermo Scientific K-Alpha XPS, Al Kα radiation). The lateral structures of the $2H/1T'MoTe_2$ were studied using a JEOL TEM 2100 operated at 200 kV.

4.3 Device fabrication and characterization.

MoTe₂ FETs: Standard photolithography and thermal evaporation processes were employed to prepare 40 nm Pd on the $MoTe_2$ arrays. After the deposition process, the samples were annealed at 200 °C for 2 h to improve the contact between $MoTe_2$ and Pd electrodes. A Keithley 4200 SCS semiconductor characterization system with a Lakeshore probe station were used to measure electrical and characterization parameters.

MoTe₂ gas sensors: To fabricate Pd-contacted and 1T′-contacted gas sensors, 2H MoTe₂ (10×5 mm) and 1T′/2H/1T′ MoTe₂ (2.5×5 mm/5×5 mm/2.5×5 mm) films were synthesized using a method described in Section 4.1. For the Pd-contacted device, Pd electrodes with 40 nm thickness were fabricated on the 2H MoTe₂ films using the thermal evaporation with a shadow mask. The channel length and width of 2H MoTe₂ were both 5 mm. For 1T′-contacted device, Pd (40 nm) electrodes were fabricated on the 1T′ MoTe₂ regions. The as-fabricated devices were connected to copper wires using the silver paste. The NH₃ sensing experiment was performed using a homemade gas sensing system[31]. In the measurement, ammonium hydroxide was delivered into the chamber's bottom using a syringe, and then reacted with potassium hydroxide to release NH₃. The chamber was kept at room temperature during the measurement. The NH₃ concentration in the chamber was determined by the volume and concentration of the liquid ammonia solution. The value was calculated using the following equation[31]:

$$C_{\text{NH}_3} = \frac{22.4 T \rho_{\text{NH}_4\text{OH}} V_{\text{NH}_4\text{OH}}}{273 MV} \times 1000 \qquad (3)$$

where C_{NH_3} is the concentration of gaseous ammonia in the Erlenmeyer flask (ppm), $\rho_{\text{NH}_4\text{OH}}$ is the density of liquid ammonia (g/mL), T is the testing temperature (298 K), M is the molecular weight of gaseous ammonia (g/mol), $V_{\text{NH}_4\text{OH}}$ is the volume of liquid ammonia (μL), and V is the volume of the Erlenmeyer flask (L). The electrical responses of MoTe₂ gas sensors to the NH₃ were measured with a Keithley 4200-SCS semiconductor testing system. A bias voltage of 1 V was applied to the devices during the measurements.

4.4 Theoretical Calculation.

Using the Quantum ATK software package and the linear combination of atomic

orbitals (LCAO) basis set, density functional theory (DFT) method was employed for geometry optimization and calculation of electronic properties. For structural relaxation, the limited-memory Broyden Fletcher Goldfarb Shanno (LBFGS) algorithm was taken into consideration. The calculations applied the double-polarized (DZP) basis set, the Perdew-Burke-Ernzerhof (PBE) exchange-correlation functional, and the general gradient approximation (GGA). The plane-wave basis set had an energy cutoff of 450 eV. During the geometry optimization, the applied force (less than 0.02 eV/Å) on each atom was adopted as a convergence criterion. For the (001) surfaces of 1T´ and 2H MoTe$_2$, 4 × 4 supercells were used, while 3 × 1 supercells were used for the (101) lattice plane of 1T´MoTe$_2$ and (100) and (010) lattice planes of 2H MoTe$_2$[39]. The 2 × 2 × 1 Monkhorst and Pack k-point sampling were also used. The convergence energy threshold for the self-consistent calculations was set as 10^{-4} eV [39]. A 15 Å vacuum space along the z direction was added to avoid the interaction of two adjacent layers. The following equation was used to calculate the gas's adsorption energy onto MoTe$_2$ [39]:

$$E_{ads} = E_{total} - E_{MoTe_2} - E_{gas} \qquad (4)$$

where E_{ads} represents the total energy of the gas adsorbed on MoTe$_2$ and E_{MoTe} and E_{gas} represent the energies of clean MoTe$_2$ and gas, respectively.

Supporting Information

Supporting Information is available from the Wiley Online Library or from the author.

Acknowledgments

Conflict of Interest

The authors declare no conflict of interest.

Author Contributions

P.A.H. conceived the idea. S.Z. conducted material synthesis experiments. Y.W. conducted the theoretical simulation. S.Z. and F.G. carried out the electrical characterizations of devices. S.Z and H.S. performed gas sensing measurements. J.Z., Z.L. Y.Q.F. and S.Z. contributed to the scientific discussions. S.Z wrote the manuscript. P.A.H. and Y.Q.F. revised the manuscript. All authors have given approval to the final version of the manuscript.

Data Availability Statement

The data that support the findings of this study are available from the corresponding author upon reasonable request

Received: ((will be filled in by the editorial staff))
Revised: ((will be filled in by the editorial staff))
Published online: ((will be filled in by the editorial staff))

Reference

[1] a) J. Kong, N. R. Franklin, C. Zhou, M. G. Chapline, S. Peng, K. Cho, H. Dai, *Science* **2000**, 287, 622; b) E. S. Snow, F. Perkins, J. A. Robinson, *Chemical Society Reviews* **2006**, 35, 790.

[2] a) P. Qi, O. Vermesh, M. Grecu, A. Javey, Q. Wang, H. Dai, S. Peng, K. Cho, *Nano Letters* **2003**, 3, 347; b) X. P. Gao, G. Zheng, C. M. Lieber, *Nano Letters* **2010**, 10, 547; c) J.-i. Hahm, C. M. Lieber, *Nano Letters* **2004**, 4, 51.

[3] M. Ganzhorn, A. Vijayaraghavan, S. Dehm, F. Hennrich, A. A. Green, M. Fichtner, A. Voigt, M. Rapp, H. von Löhneysen, M. C. Hersam, *ACS Nano* **2011**, 5, 1670.

[4] F. Schedin, A. K. Geim, S. V. Morozov, E. W. Hill, P. Blake, M. I. Katsnelson, K. S. Novoselov, *Nature Materials* **2007**, 6, 652.

[5] O. Lopez-Sanchez, D. Lembke, M. Kayci, A. Radenovic, A. Kis, *Nature Nanotechnology* **2013**, 8, 497.

[6] Y. Kim, S.-K. Kang, N.-C. Oh, H.-D. Lee, S.-M. Lee, J. Park, H. Kim, *ACS Applied Materials & Interfaces* **2019**, 11, 38902.

[7] D. J. Late, T. Doneux, M. Bougouma, *Applied Physics Letters* **2014**, 105, 233103.

[8] X. Chen, J. Hu, P. Chen, M. Yin, F. Meng, Y. Zhang, *Sensors and Actuators B: Chemical* **2021**, 339, 129902.

[9] Z. Lu, Y. Zhai, Q. Liang, W. Wu, *Chemical Physics Letters* **2020**, 755, 137737.

[10] S. Nakaharai, M. Yamamoto, K. Ueno, K. Tsukagoshi, *ACS Applied Materials & Interfaces* **2016**, 8, 14732.

[11] a) X. Xu, S. Liu, B. Han, Y. Han, K. Yuan, W. Xu, X. Yao, P. Li, S. Yang, W. Gong, *Nano Letters* **2019**, 19, 6845; b) S. Yang, X. Xu, W. Xu, B. Han, Z. Ding, P. Gu, P. Gao, Y. Ye, *ACS Applied Nano Materials* **2020**, 3, 10411.

[12] a) J. H. Sung, H. Heo, S. Si, Y. H. Kim, H. R. Noh, K. Song, J. Kim, C.-S. Lee, S.-

Y. Seo, D.-H. Kim, *Nature Nanotechnology* **2017**, 12, 1064; b) R. Ma, H. Zhang, Y. Yoo, Z. P. Degregorio, L. Jin, P. Golani, J. Ghasemi Azadani, T. Low, J. E. Johns, L. A. Bendersky, *ACS Nano* **2019**, 13, 8035.

[13] Z. Xie, W. Lei, W. Zhang, Y. Liu, L. Yang, X. Wen, H. Chang, *Advanced Materials Interfaces* **2021**, 8, 2002023.

[14] a) L. Zhou, A. Zubair, Z. Wang, X. Zhang, F. Ouyang, K. Xu, W. Fang, K. Ueno, J. Li, T. Palacios, *Advanced Materials* **2016**, 28, 9526; b) Q. Zhang, X.-F. Wang, S.-H. Shen, Q. Lu, X. Liu, H. Li, J. Zheng, C.-P. Yu, X. Zhong, L. Gu, *Nature Electronics* **2019**, 2, 164.

[15] L. Yang, W. Zhang, J. Li, S. Cheng, Z. Xie, H. Chang, *ACS Nano* **2017**, 11, 1964.

[16] L. Zhou, K. Xu, A. Zubair, A. D. Liao, W. Fang, F. Ouyang, Y.-H. Lee, K. Ueno, R. Saito, T. Palacios, *Journal of the American Chemical Society* **2015**, 137, 11892.

[17] M. Camacho-López, L. Escobar-Alarcón, M. Picquart, R. Arroyo, G. Córdoba, E. Haro-Poniatowski, *Optical Materials* **2011**, 33, 480.

[18] X. Xu, S. Chen, S. Liu, X. Cheng, W. Xu, P. Li, Y. Wan, S. Yang, W. Gong, K. Yuan, *Journal of the American Chemical Society* **2019**, 141, 2128.

[19] S. Cho, S. Kim, J. H. Kim, J. Zhao, J. Seok, D. H. Keum, J. Baik, D.-H. Choe, K. J. Chang, K. Suenaga, *Science* **2015**, 349, 625.

[20] Y. Yoo, Z. P. DeGregorio, Y. Su, S. J. Koester, J. E. Johns, *Advanced Materials* **2017**, 29, 1605461.

[21] S. Zhang, F. Gao, W. Feng, H. Yang, Y. Hu, J. Zhang, H. Xiao, Z. Li, P. Hu, *Nanotechnology* **2021**, 33, 105301.

[22] L. Ma, J. Zhu, W. Li, R. Huang, X. Wang, J. Guo, J.-H. Choi, Y. Lou, D. Wang, G. Zou, *Journal of the American Chemical Society* **2021**, 143, 13314.

[23] F. Gao, H. Chen, W. Feng, Y. Hu, H. Shang, B. Xu, J. Zhang, C. Y. Xu, P. Hu,

Advanced Functional Materials **2021**, 31, 2104359.

[24]X. Zhang, Z. Jin, L. Wang, J. A. Hachtel, E. Villarreal, Z. Wang, T. Ha, Y. Nakanishi, C. S. Tiwary, J. Lai, *ACS Applied Materials & Interfaces* **2019**, 11, 12777.

[25]M. S. Choi, N. Ali, T. D. Ngo, H. Choi, B. Oh, H. Yang, W. J. Yoo, *Advanced Materials* **2022**, 2202408.

[26]W. Zheng, Y. Xu, L. Zheng, C. Yang, N. Pinna, X. Liu, J. Zhang, *Advanced Functional Materials* **2020**, 30, 2000435.

[27]B. Shao, Y. Liu, X. Zhuang, S. Hou, S. Han, X. Yu, J. Yu, *Journal of Materials Chemistry C* **2019**, 7, 10196.

[28]A. M. Afzal, M. Z. Iqbal, G. Dastgeer, G. Nazir, S. Mumtaz, M. Usman, J. Eom, *ACS Applied Materials & Interfaces* **2020**, 12, 39524.

[29]S. Wei, C. Ge, L. Zhou, S. Zhang, M. Dai, F. Gao, Y. Sun, Y. Qiu, Z. Wang, J. Zhang, *ACS Applied Electronic Materials* **2019**, 1, 2380.

[30]J. Qiu, X. Xia, Z. Hu, S. Zhou, Y. Wang, Y. Wang, R. Zhang, J. Li, Y. Zhou, *Nanotechnology* **2021**, 33, 065501.

[31]W. Wang, Y. Zhen, J. Zhang, Y. Li, H. Zhong, Z. Jia, Y. Xiong, Q. Xue, Y. Yan, N. S. Alharbi, *Sensors and Actuators B: Chemical* **2020**, 321, 128471.

[32]S. Singh, J. Deb, U. Sarkar, S. Sharma, *ACS Sustainable Chemistry & Engineering* **2021**, 9, 7328.

[33]S. Kanaparthi, S. G. Singh, *ACS Sustainable Chemistry & Engineering* **2021**, 9, 14735.

[34]M. Yang, C. Au, G. Deng, S. Mathur, Q. Huang, X. Luo, G. Xie, H. Tai, Y. Jiang, C. Chen, *ACS Applied Materials & Interfaces* **2021**, 13, 52850.

[35]X. Li, X. Li, Z. Li, J. Wang, J. Zhang, *Sensors and Actuators B: Chemical* **2017**, 240, 273.

[36] Y. Zhu, C. Chen, S. Wu, R. Cheng, J. Gao, Y. Yu, W. Zhou, *ACS Applied Nano Materials* **2021**, 4, 1976.

[37] W. Jiao, J. He, L. Zhang, *Journal of Alloys and Compounds* **2022**, 895, 162561.

[38] H. Meng, W. Yang, K. Ding, L. Feng, Y. Guan, *Journal of Materials Chemistry A* **2015**, 3, 1174.

[39] B. Zong, Q. Li, X. Chen, C. Liu, L. Li, J. Ruan, S. Mao, *ACS Applied Materials & Interfaces* **2020**, 12, 50610.

[40] B. Liu, L. Chen, G. Liu, A. N. Abbas, M. Fathi, C. Zhou, *ACS Nano* **2014**, 8, 5304.

The table of contents entry

Compared to the other types of gas sensors, our 1T´/2H/1T´ device possesses distinctive advantages. Firstly, the polycrystalline 2H MoTe$_2$ provides numerous defects, such as vacancies, edges, and grain boundaries, which play crucial roles in enhancing the response rate and sensitivity of a gas sensor. Secondly, the low-resistance planar heterostructure ensures a microamp scale current output even at larger channel aspect ratios.

Shichao Zhang, You Wu, Feng Gao, Huiming Shang, Jia Zhang, Zhonghua Li, YongQing Fu, and PingAn Hu*

Title:
Field effect transistor sensors based on in-plane 1T´/2H/1T´ MoTe$_2$ heterophases with superior sensitivity and output signals

ToC figure